DE GRUYTER Z. Phys. Chem. 2020; 234(6): 1155–1169

Thorsten Cottre, Katharina Welter, Emanuel Ronge,
Vladimir Smirnov, Friedhelm Finger, Christian Jooss,
Bernhard Kaiser* and Wolfram Jaegermann

Integrated Devices for Photoelectrochemical Water Splitting Using Adapted Silicon Based Multi-Junction Solar Cells Protected by ALD TiO_2 Coatings

https://doi.org/10.1515/zpch-2019-1483
Received May 16, 2019; accepted November 4, 2019

Abstract: In this study, we present different silicon based integrated devices for photoelectrochemical water splitting, which provide enough photovoltage to drive the reaction without an external bias. Thin films of titanium dioxide, prepared by atomic layer deposition (ALD), are applied as a surface passivation and corrosion protection. The interfaces between the multi-junction cells and the protective coating were optimized individually by etching techniques and finding optimal parameters for the ALD process. The energy band alignment of the systems was studied by X-ray photoelectron spectroscopy (XPS). Electrochemically deposited platinum particles were used to reduce the HER overpotential. The prepared systems were tested in a three-electrode arrangement under AM 1.5 illumination in 0.1 M KOH. In final tests the efficiency and stability of the prepared devices were tested in a two-electrode arrangement in dependence of the pH value with a ruthenium-iridium oxide counter electrode. For the tandem-junction device solar to hydrogen efficiencies (STH) up to 1.8% were reached, and the triple-junction device showed a maximum efficiency of 4.4%.

Keywords: band alignment; photoelectrochemical cell; photoelectron spectroscopy.

***Corresponding author: Bernhard Kaiser,** Institute of Material Science, Technische Universität Darmstadt, D-64287 Darmstadt, Germany, e-mail: kaiser@surface.tu-darmstadt.de
Thorsten Cottre and Wolfram Jaegermann: Institute of Material Science, Technische Universität Darmstadt, D-64287 Darmstadt, Germany
Katharina Welter, Vladimir Smirnov and Friedhelm Finger: IEK5-Photovoltaics, Forschungszentrum Jülich, D-52425 Jülich, Germany
Emanuel Ronge and Christian Jooss: Institute for Material Physics, Universität Göttingen, Friedrich-Hund-Platz 1, D-37077 Göttingen, Germany

1 Introduction

The progress of climate change and the increased demand for energy sources require a sustainable energy system. Since the availability of renewable energy sources, such as solar and wind energy, is limited, efficient energy storage technologies are needed. In this context, photoelectrochemical water splitting is a very promising alternative to conventional energy storage technologies due to the high mass-related energy density of hydrogen [1]. Solar driven water splitting uses semiconductors as a light absorbing material to generate charge carriers, which leads in the case of a photocathode to the hydrogen evolution reaction (HER) at the semiconductor-electrolyte interface. The oxygen evolution reaction (OER) takes place at the associated anode. The thermodynamic voltage to initiate the water splitting reaction is 1.23 V. Due to kinetic inhibition this voltage is not high enough to drive the reaction. Consequently, in addition to the development of adapted photoabsorbers the design of advanced electrocatalysts is important for the overall efficiency of integrated devices. Furthermore, a suitable band alignment of the semiconductor component and an appropriate coupling of an active electrocatalyst are crucial to reduce internal resistances for charge carrier transport. Moreover, the individual components must be arranged in a defined order to enable efficient and cost-effective device integration.

The use of silicon as a light absorbing semiconductor enables the development of highly efficient and inexpensive devices since silicon is well studied, technologically established and earth abundant. In the past efficiencies around 9.5% were achieved by using silicon based multi-junction cells as buried-junction photocathodes [2]. The main hindrance for the use of silicon for solar driven water splitting is the instability in aqueous alkaline and acidic electrolyte solutions. One strategy to overcome this problem is to apply a protection layer on the semiconductor device [3, 4]. So far, the most promising material which combines electrochemical stability in corrosive media and electrical conductivity is titanium dioxide [5]. In previous studies the successful surface passivation and long-term stability of titanium dioxide deposited on silicon and III-V semiconductors could be shown [6, 7]. The use of a suitable deposition method is of decisive importance in the development of protective coatings. Here the advantages of atomic layer deposition (ALD) offer a relevant benefit by controlling the layer growth on an atomic level [8, 9]. Beyond that, the sequential, self-limited layer growth enables the generation of highly conformal layers. Thus, the ALD coating process sets itself apart from other deposition and encapsulation techniques. Additionally, the deposition onto textured and rougher surfaces is possible. In this study we use ALD to produce thin titanium dioxide films as protective coatings for silicon based multi-junction solar cells used as buried-junction photocathodes. By combining high photovoltages of a-Si:H/a-Si:H tandem cells and a-Si:H/a-Si:H/µc-Si:H triple cells with ALD-TiO_2 and a particulate platinum electrocatalyst the preparation of integrated devices is possible, which are able to split water without an external bias. In this study, the focus is on the interfaces of the silicon solar cells and the titanium dioxide passivation layer. In order to investigate the influence of the interface on the device performance no ZnO:Al/Ag back contact was used [2]. This contact is usually applied to allow better light trapping which leads to higher efficiencies, therefore in this study lower efficiencies are expected.

The deposition of TiO_2 was performed in a home-built UHV-compatible thermal ALD reactor, which is connected to an integrated XPS/UPS system. The precursors used for the ALD process were titanium tetrachloride and water as an oxygen source. The use of X-ray photoelectron spectroscopy (XPS) offers the possibility to determine the electronic structure of the contacts that arise between the individual components which is a significant advantage in device integration. XPS is a surface sensitive method and therefore ideally suited to follow small changes in the surface composition before and after the electrochemistry (EC) experiments. For optimizing the electronic contact properties of the interfaces formed between the multi-junction solar cells and the passivation layer different etching techniques were tested. The energy band alignments of the prepared systems were studied by XPS and the performance of the photocathodes

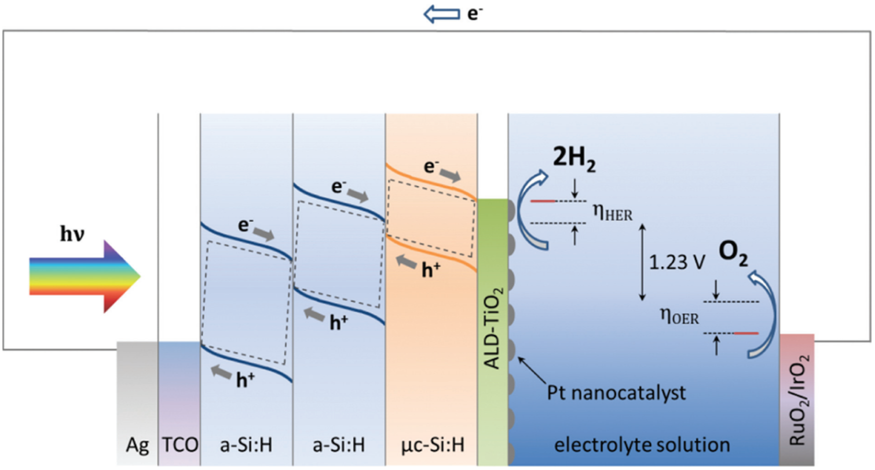

Fig. 1: Scheme of the energetics of the integrated triple-junction device for photoelectrochemical water splitting with a a-Si:H/a-Si:H/µc-Si:H solar cell passivated by ALD-TiO_2 and decorated with Pt nanoparticles for the HER and a ruthenium-iridium dioxide OER electrode.

were measured under working conditions in a three-electrode setup under AM 1.5 illumination. In a next step, two-electrode arrangements were set up to test the efficiency and stability of the complete devices under real conditions including both half-cell reactions. As the OER catalyst a ruthenium-iridium oxide electrode was used. It was found that the integrated devices show a strong dependence of the pH value, while for both test arrangements the highest solar to hydrogen efficiencies (STH) were reached in concentrated acid. The device including the tandem-junction (a-Si:H/a-Si:H/TiO_2/Pt) showed a maximum STH efficiency of 1.8%, while the addition of another microcrystalline silicon junction (a-Si:H/a-Si:H/μc-Si:H/TiO_2/Pt) increased the efficiency to 4.4%. A scheme of the integrated triple-junction device is shown in Figure 1.

2 Experimental methods

2.1 Preparation of integrated devices

The silicon based multi-junction cells were prepared by plasma enhanced chemical vapor deposition (PECVD) on glass covered with fluorine doped tin oxide (FTO) in a stacked p-i-n superstrate configuration. For more detailed information about the preparation process and the cell configuration see [2] and [10]. For further device integration 1×1 cm^2 samples were used. The a-Si:H/a-Si:H tandem cells have a n-doped a-Si:H back contact. Due to storage and handling in air a thin SiO_x layer can be formed at the a-Si:H surface. In order to remove the thin SiO_x layer and to restore the initial a-Si:H layer, the tandem cells were etched for 5 min with ammonium fluoride (40%, semiconductor grade VLSI PURANAL, Sigma-Aldrich), rinsed with Milli-Q water and dried in a nitrogen flow. The a-Si:H/a-Si:H/μc-Si:H triple-junction cells possess a n-doped μc-SiO_x layer as contact [11]. The samples were etched in a piranha bath using sulfuric acid (96%, VLSI Selectipur, BASF) and hydrogen peroxide (31%, VLSIn Selectipur, BASF) in a defined ratio (H_2SO_4:H_2O_2 = 3:1) for 5 min to remove carbon impurities from the surface. Ammonium fluoride was not used in this case in order to keep the as deposited n-doped μc-SiO_x layer intact. Afterwards the samples were also rinsed with Milli-Q water and dried in a nitrogen flow. After the etching procedures the samples were transported in a nitrogen atmosphere and transferred immediately to the ultra-high vacuum (UHV) system. In a next step, the samples were transported within our integrated UHV system to the ALD reactor. The TiO_2 deposition was performed by using titanium tetrachloride (99.995%, Sigma-Aldrich) and Milli-Q water as precursors with nitrogen as a purging gas and ALD cycle numbers of 100, 200 and

300 at a growth temperature of 160 °C. More experimental details will be given in a forthcoming publication [12]. To reduce the overpotential for the HER a particulate platinum electrocatalyst was applied on the TiO_2 layer. The Pt deposition was performed galvanostatically with a current density of -0.5 mA cm^{-2} for 120 s in a three-electrode setup with a silver/silverchloride (3 M NaCl) reference electrode and a platinum wire as a counter electrode from a 2 mM K_2PtCl_4 (99%, Carbolution Chemicals GmbH) in 0.5 M H_2SO_4 (Carl Roth GmbH) solution under AM 1.5 illumination.

2.2 Interface studies and spectra analysis

In order to study the electronic structures of the prepared systems XPS measurements were performed after each preparation step. The transfer of the samples after TiO_2 deposition to the analysis chamber was carried out without breaking the UHV. The XPS analysis chamber is equipped with a SPECS Phoibos 150 analyzer and a SPECS Focus 500 X-ray source using the monochromatized AlKα line at 1486.74 eV. At first the samples were measured before and after the etching procedures. The next measurements were performed after the interface formation of the TiO_2 passivation layer with the corresponding solar cell. The ALD cycle number was set to 100 for the tandem-junction device and 80 for the triple-junction device, leading to a layer thickness of 6.6 nm and 4.8 nm, respectively. The reduced ALD cycle number for the triple-junction device is important to keep the µc-Si:H visible in XPS after the TiO_2 deposition. The last XPS measurements were performed after the Pt deposition with a 10 mM K_2PtCl_4 in 0.5 M H_2SO_4 solution with the same parameters as described above. In XPS the incident photons lead to a systematic shift in binding energy for all measurements due to the light induced photovoltage of the silicon solar cells, so a clear signal of Pt in XPS is advantageous to correct the XPS spectrum using the valence band spectrum of Pt. For all core-level measurements the backgrounds are substracted using the Shirley algorithm [13]. The layer thickness of SiO_x was calculated using the electron attenuation length obtained by Hill et al. [14].

2.3 Photoelectrochemical characterization

The photoelectrochemical performance of the prepared devices were tested in a three-electrode arrangement in 0.1 M KOH (±0.2%, Carl Roth GmbH) by using cyclic voltammetry and chronopotentiometry under AM 1.5 illumination. In order to form an ohmic contact to the transparent conductive oxide (TCO) the solar cells were scratched and contacted with colloidal silver paste (Ted pella Inc). All photoelectrochemical experiments were measured in a Zahner PECC-2 cell with a Gamry potentiostat (Interface 1000) and sample areas of 0.5 cm^2. As reference electrode a silver/silverchloride electrode (3 M NaCl) was used while a Pt wire served as counter electrode. The used full spectrum solar simulator was equipped with a 150 W Xe short arc lamp (LS0108, LOT-QuantumDesign GmbH). In a next step a two-electrode setup was built by using the prepared photocathodes and a commercial ruthenium-iridium oxide counter electrode (Metakem GmbH) for the OER. These measurements were performed in a modified Zahner PECC-2 cell in alkaline (0.1 M and 1 M KOH ($\pm$0.2%, Carl Roth GmbH)) and acidic (0.1 M and 1 M H_2SO_4 ($\pm$0.2%, Carl Roth GmbH)) electrolyte solutions. The thickness of the TiO_2 passivation layer was 6.6 nm for all measurements in a two-electrode arrangement. Linear sweep voltammetry and chronoamperometry were used for the determination of the efficiency and stability of the integrated devices under AM 1.5 illumination.

3 Results

3.1 Interface engineering

For the determination of the electronic structure of the integrated devices interface experiments were performed. XPS measurements were conducted after each preparation step. Figure 2 summarizes the measurements for both studied systems, the a-Si:H/a-Si:H/TiO_2/Pt tandem-junction device and the a-Si:H/a-Si:H/µc-Si:H/TiO_2/Pt triple-junction device.

For both systems the core-level lines and the valence band spectra are shifted to lower binding energies due to the incoming photons during the XPS measurements, which lead to an induced photovoltage in the silicon solar cells. This effect was already observed in previous studies for a-Si:H/a-Si:H photoelectrodes protected by sputtered TiO_2 [15]. In this work the photovoltage shift for the a-Si:H/a-Si:H cell is 0.88 eV and for the a-Si:H/a-Si:H/µc-Si:H cell 0.12 eV.

In the first step the a-Si:H/a-Si:H cell was etched with NH_4F (40%) for 5 min. In Figure 2a the successful removal of the native silicon oxide can be seen in the O 1s and Si 2p peak, only a small amount of oxygen can be detected after the etching procedure. The atomic layer deposition of TiO_2 leads to the typical signal for the O 1s and the Ti 2p peak. The uncorrected peak position of the O 1s is 529.7 eV and the Ti $2p_{3/2}$ and Ti $2p_{1/2}$ are located at 458.2 eV and 463.9 eV, respectively. Moreover the Ti 2p peak possesses an asymmetric line shape indicating formation of Ti^{3+} species, resulting in a n-doping of the titanium dioxide. In the Si 2p signal the formation of a thin SiO_x layer ($\approx$1 nm) can be seen, which can be

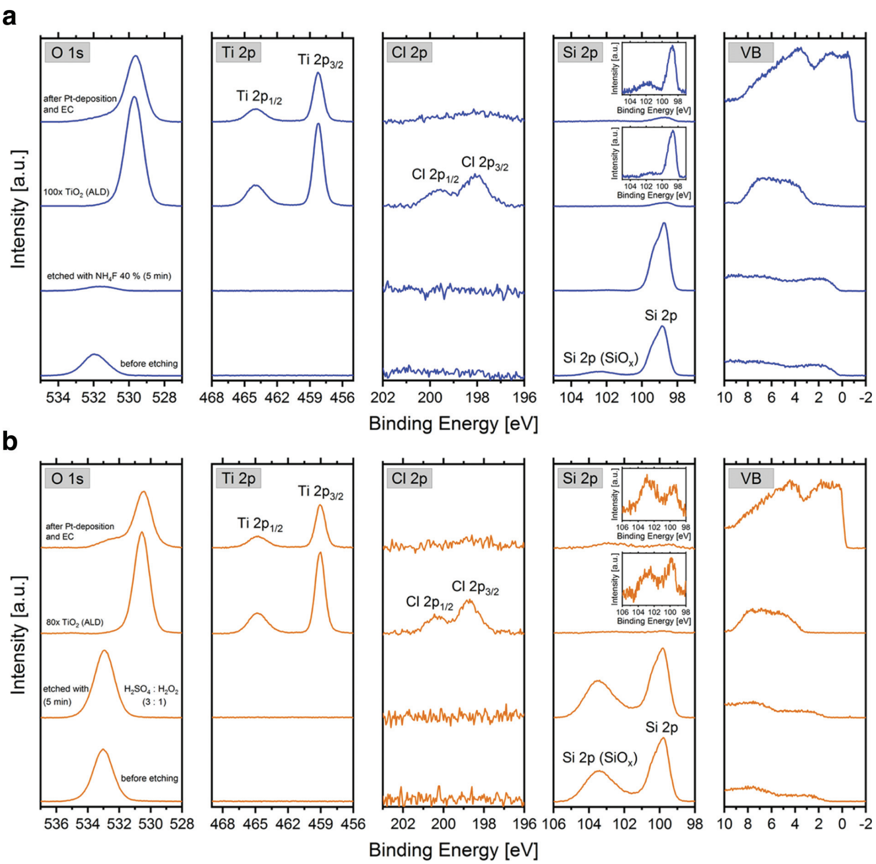

Fig. 2: Interface engineering of the integrated devices (XPS characterization) (a) Interface formation of a-Si:H/a-Si:H tandem cell and ALD-TiO_2: 1. XP spectrum: before etching, 2. XP spectrum: after etching with NH_4F (40%) for 5 min, 3. XP spectrum: 100 ALD cycles of TiO_2, 4. XP spectrum: electrodeposition of Pt nanoparticles and EC, (b) Interface formation of a-Si:H/a-Si:H/µc-Si:H triple cell and ALD-TiO_2: 1. XP spectrum: before etching, 2. XP spectrum: after etching with piranha solution for 5 min, 3. XP spectrum: 80 ALD cycles of TiO_2, 4. XP spectrum: electrodeposition of Pt nanoparticles and EC. The Cl 2p line is presented with an intensity factor of 17 for (a) and 20 for (b). The Si 2p line is presented with an intensity factor of 1.5 for (a) and 4 for (b). The insets are magnifications of the Si 2p peaks with an intensity factor of 19 (for 3.) and 17 (for 4.) for (a) and 67 (for 3.) and 24 (for 4.) for (b). All intensity factors are related to the O 1s line.

explained by a reoxidation during the first ALD cycles. Furthermore a peak shift of the Si $2p_{3/2}$ component of 100 meV from 98.7 eV to 98.6 eV can be observed. Additionally, we found chlorine impurities in both systems (≈2% at. conc.) caused by the used precursor. For the ALD process based on titaniumtetrachloride and water the implementation of chlorine was already described by Aarik et al. [16]. Ritala et al. found a similar content of chlorine in the films for a comparable growth temperature of 150 °C [17]. After the platinum deposition and photoelectrochemical measurements in 0.1 M KOH including a galvanostatic stability measurement for 1 h with a current density of -2 mA cm^{-2} the titanium dioxide film is still intact, but a further oxidation of the silicon can be observed in the Si 2p peak. Otherwise adsorbed water species in the O 1s peak around 532.0 eV and a decreased chlorine content can be detected as well as the metallic component of platinum in the valence band spectrum.

In contrast to the tandem cell, the preparation of the triple cell system started with an etching procedure in a piranha bath for 5 min (Figure 2b). The removal of the carbon impurities on the silicon surface leads to a slightly higher intensity of the O 1s peak of the n-doped µc-SiO_x:H at 533.0 eV, no other significant changes in the spectra can be found. Also for this system the typical peak positions of the O 1s at 530.6 eV, the Ti $2p_{3/2}$ at 459.1 eV and Ti $2p_{1/2}$ at 464.8 eV can be found after the ALD deposition of TiO_2 as well as the same n-doping in the TiO_2 and chlorine impurities. For the location of the Si 2p signal of the µc-Si:H no relevant changes in binding energy can be observed after TiO_2 deposition, the Si $2p_{3/2}$ signal is still located at 99.8 eV. Because of that a pinned contact of the µc-Si:H and the µc-SiO_x:H can be concluded. After the electrodeposition of platinum and the electrochemical investigations similar observations can be seen concerning the adsorption of water, the removal of chlorine and the metallic contributions of platinum in the valence band. Otherwise a stronger degradation of the TiO_2 passivation layer can be seen in the O 1s peak around 533.0 eV due to an increased signal of SiO_x.

The results of the interface engineering of the two different contacts are summarized in Figure 3 describing the electronic structure in the form of energy band diagrams. The bandgap of ALD-TiO_2 was determined by us to 3.4 eV using XPS for the valence band position and a Mott-Schottky analysis for the location of the conduction band. The bandgap of a-Si:H is assumed to be 1.9 eV and of µc-Si:H 1.1 eV. The corresponding dopings are known from the parameters of the preparation process.

The interface between the a-Si:H/a-Si:H tandem cell (Figure 3a) and the ALD-TiO_2 protective coating contains a SiO_x intermediate layer with a layer thickness of about 1 nm. The conduction band offset for the electron transfer across the interface is 0.8 eV due to an induced upward band bending in the a-Si:H bottom cell. Similar observations were made for amorphous and crystalline silicon protected by sputtered TiO_2 [15, 18]. However, considering the small thickness of the SiO_x intermediate layer a tunnelling process across the interface is possible [19, 20]. Nevertheless, a loss can be expected for the generated photoelectrons, which can

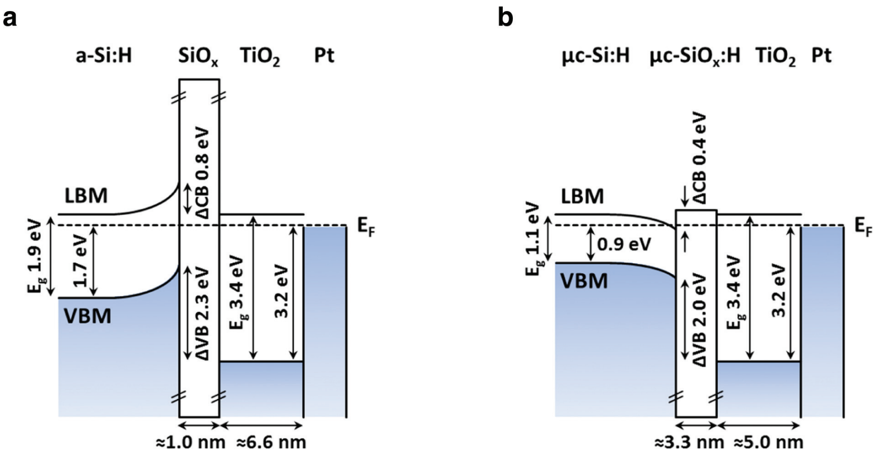

Fig. 3: Energy band diagrams of the integrated devices (a) Interface of the a-Si:H/a-Si:H/TiO_2/Pt tandem-junction system, (b) Interface of the a-Si:H/a-Si:H/µc-Si:H/TiO_2/Pt triple-junction system.

lower the efficiency of the integrated device. Besides the kinetic hindrance at the platinum electrocatalyst an internal electrical resistance of the ALD-TiO_2 can be present, but the performance loss across the TiO_2 passivation layer is not expected to be decisive due to the intrinsic n-doping. In contrast to the tandem cell device the a-Si:H/a-Si:H/µc-Si:H triple cell (Figure 3b) possesses a slight downward band bending in the µc-Si:H bottom cell caused by an initial Fermi level pinning at the µc-SiO_x:H layer. The thickness of the µc-SiO_x:H layer is about 3.3 nm. The conduction band offset of the µc-Si:H with respect to the n-doped µc-SiO_x:H can be calculated to 0.4 eV and therefore offers good contact properties for electron transfer to the ALD-TiO_2 layer. From this we can conclude only a minor performance loss of the triple cell device caused by interface effects.

3.2 Photoelectrochemical characterization

After evaluating the electronic structure of the integrated devices further photoelectrochemical measurements were conducted in a 3-electrode arrangement in 0.1 M KOH under AM 1.5 illumination with varied TiO_2 layer thicknesses. The respective results of both prepared systems are summarized in Figure 4. For the investigation of the overall efficiency of the devices in dependence of the TiO_2 layer thickness, cyclic voltammograms (Figure 4a) were recorded for devices prepared with 100 and 300 ALD-TiO_2 cycles. The corresponding layer thicknesses are

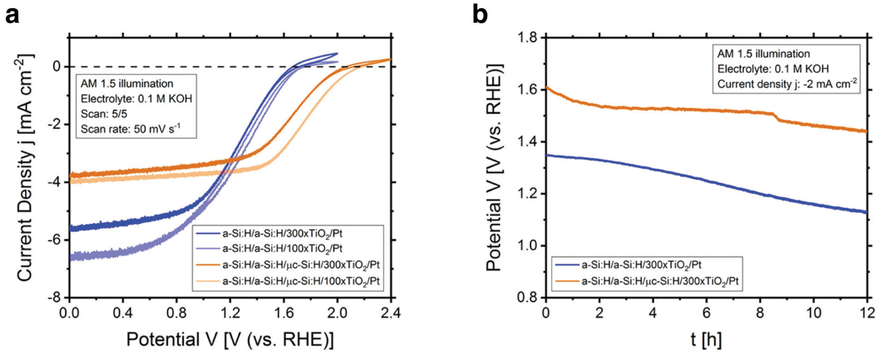

Fig. 4: Photoelectrochemical charaterization of the integrated devices (3-electrode setup) (a) cyclic voltammetry of the tandem- and triple-junction devices in 0.1 M KOH under AM 1.5 illumination, (b) chronopotentiometry ($j = -2$ mA cm^{-2}) of the tandem- and triple-junction devices in 0.1 M KOH under AM 1.5 illumination.

6.6 nm and 30.5 nm based on the growth rate of the ALD process. The scan rate has been set to 50 mV s^{-1} and the last of 5 scans is shown.

While for the a-Si:H/a-Si:H tandem-junction devices the onset for the HER is at 1.7 V vs. RHE for both TiO_2 passivation layer thicknesses, a clear decrease in the saturation current density can be observed from −6.6 mA cm^{-2} (6.6 nm TiO_2) to −5.6 mA cm^{-2} (30.5 nm TiO_2) at 0 V vs. RHE. Furthermore, it is noticeable that the gradient of both samples behaves similar at higher potentials above 1 V vs. RHE with just a small shift in the potential. The highest performance losses are below 1 V vs. RHE due to the increased resistance of the thicker TiO_2 passivation layer. For the a-Si:H/a-Si:H/µc-Si:H triple-junction devices a small shift in the HER onset potential from 2.2 V vs. RHE (6.6 nm TiO_2) to 2.1 V vs. RHE (30.5 nm TiO_2) and a minor decrease in the saturation current density from −4.0 mA cm^{-2} (6.6 nm TiO_2) to −3.8 mA cm^{-2} (30.5 nm TiO_2) can be observed. Moreover, a certain decrease in the fill factor can be seen due to the increased resistance of the thicker TiO_2 passivation layer. Figure 4b shows the chronopotentiometry measurements at a current density of −2 mA cm^{-2} (12 h) for both multi-junction systems prepared with 300 ALD cycles. The stabilization of the multi-junction devices with 30.5 nm ALD-TiO_2 and a platinum electrocatalyst could be carried out successfully for 12 h but both devices showed a continuous drop in the potential. The potential loss after 12 h CP is 219 mV for the tandem cell and 168 mV for the triple cell. According to this a progressive degradation of the systems can be concluded. XPS measurements (Figure 5) conducted after ALD-TiO_2 deposition and the photoelectrochemical stability measurements confirm a degradation of both prepared systems.

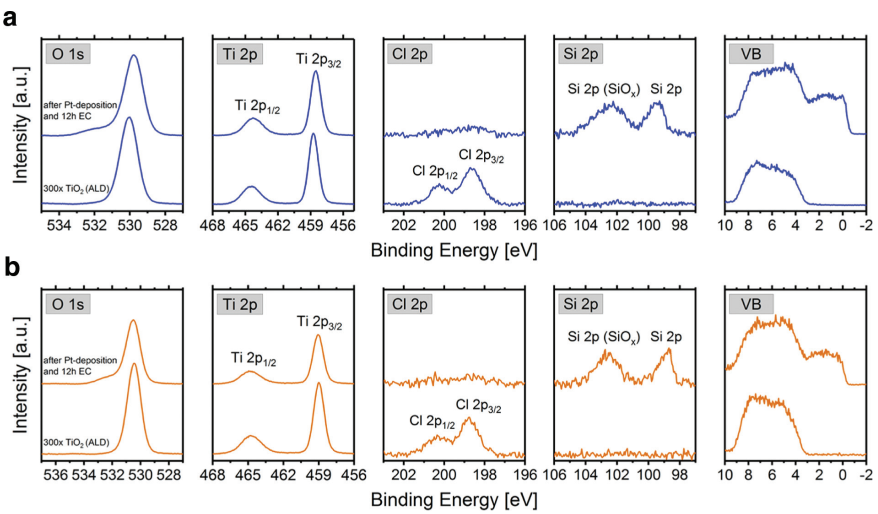

Fig. 5: Stability of the integrated devices after 12 h EC in 0.1 M KOH (XPS characterization) (a) a-Si:H/a-Si:H tandem cell: 1. XP spectrum: 300 ALD cycles of TiO_2, 2. XP spectrum: electrodeposition of Pt nanoparticles and 12 h EC, (b) a-Si:H/a-Si:H/µc-Si:H triple cell: 1. XP spectrum: 300 ALD cycles of TiO_2, 2. XP spectrum: electrodeposition of Pt nanoparticles and 12 h EC. The Cl 2p line is presented with an intensity factor of 29 for (a) and b). The Si 2p line is presented with an intensity factor of 38 for (a) and 40 for (b). All intensity factors are related to the O 1s line.

The degradation of both systems leads to an uncovering of the SiO_x/Si structure visible in the O 1s and Si 2p core level signals (Figure 5a and b). However, it can be seen from the XPS measurements that the TiO_2 passivation layer of both samples is still present. The decrease of the Ti 2p peak intensity is mainly caused by the Pt deposition and ubiquitous carbon contaminations. Nevertheless, there may be local surface defects in the TiO_2 that serve as weak spots, allowing an initial degradation to form TiO_2 patches. For a more detailed study on the formation of etching pits refer to [21]. Furthermore, a removal of the chlorine after the electrochemical measurements can be determined here as well. Likewise, the metallic signals of the deposited platinum can be found in the valence band spectrum. It could be that the removal of the chlorine leads to the generation of surface defects. Another plausible explanation for the degradation could be an inhomogeneous distribution of the Pt nanoparticles which may cause areas with low Pt coverage.

In literature a successful long-term test for 82 days of a TiO_2:H protected crystalline Si-based photocathode is reported [22]. The conclusion of Bae et al. with regard to the performance loss was that carbon contaminations block catalytically active centers of the surface.

To study the performance of the integrated devices under real conditions two-electrode measurements were conducted including the prepared buried-junction photocathodes and a RuO_2/IrO_2 OER catalyst as a function of pH. To identify the maximum achievable efficiencies of these types of devices higher concentrated eletrolyte solutions and thinner TiO_2 passivation layers have been employed, altough we exptected a reduced stability under these conditions. From the Pourbaix diagram of TiO_2 we expect a better stability of the devices under alkaline conditions [23].

Firstly, linear sweep voltammetry was used for the investigation of the onset behaviour and finding of the operating point for bias-free photoelectrochemical water splitting under various pH. Secondly, the stability at the operating point was studied using chronoamperometry for 10 min. The respective results are summarized in Figure 6 for both types of photocathodes. For the calculation of the solar to hydrogen efficiency (STH) the photocurrent density j_{op} at 0 V vs. RuO_2/IrO_2 was used. The estimation of the STH efficiency was performed with the assumption of 100% faradaic efficieny using the following equation [24]:

$$\eta_{\text{STH}} = \frac{\text{power out}}{\text{power in}} = \frac{\Delta E \cdot j_{op}}{100 \ \text{mW cm}^{-2}}. \tag{1}$$

ΔE (1.23 V) is the thermodynamic voltage required for water electrolysis under standard conditions, j_{op} is the operating current density at 0 V vs. RuO_2/IrO_2 while the input power is the incident light intensity of 100 mW cm^{-2} for AM 1.5. To consider the influence of the electrolyte, electrochemical impedance spectroscopy was used for the determination of the electrolyte resistance. The values of the individual measurements are 6.1 Ω (1 M H_2SO_4), 11.9 Ω (1 M KOH), 52.2 Ω (0.1 M H_2SO_4) and 105.6 Ω (0.1 M KOH).

The linear sweep voltammograms of the tandem- and the triple-junction devices show a similar behaviour with respect to the pH dependency (Figure 6a and b). However, the current-voltage behavior is influenced by the number of absorber subcells. The onset of the tandem-junction device is at 0.5 V vs. RuO_2/IrO_2 while the onset of the triple-junction device is at 0.8 V vs. RuO_2/IrO_2. Furthermore, it can be seen that the saturation current density starts at −1 V vs. RuO_2/IrO_2 for the tandem cell and at approximately −0.5 V vs. RuO_2/IrO_2 for the triple cell. Otherwise, it is noticeable that the slope of the measurements is significantly influenced by the used electrolyte. As expected from literature, the data show the influence of the electrolyte on the HER reaction kinetics. Although 1 M KOH has lower electrolyte resistance than 0.1 M H_2SO_4, both systems have an operating point at higher current densities for 0.1 M H_2SO_4. This can be explained by faster HER kinetics at the platinum particle catalyst in acidic environment [25]. The highest solar to hydrogen efficiencies (STH) of 1.8% for the

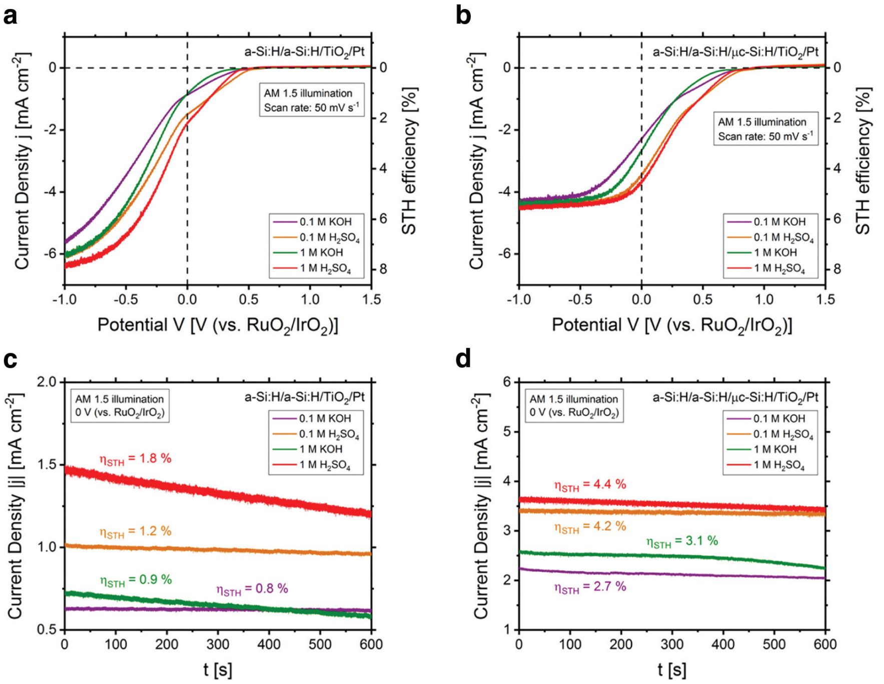

Fig. 6: Photoelectrochemical charaterization of the integrated devices (2-electrode setup) with a ruthenium-iridium OER electrode in 0.1 M and 1 M KOH and 0.1 M and 1 M H_2SO_4 under AM 1.5 illumination (a) linear sweep voltammetry of the a-Si:H/a-Si:H/TiO_2/Pt tandem-junction device, (b) linear sweep voltammetry of the a-Si:H/a-Si:H/μc-Si:H/TiO_2/Pt triple-junction device, (c) chronoamperometry of the a-Si:H/a-Si:H/TiO_2/Pt tandem-junction device, (d) chronoamperometry of the a-Si:H/a-Si:H/μc-Si:H/TiO_2/Pt triple-junction device.

tandem-junction device and 4.4% for the triple-junction device were achieved in 1 M H_2SO_4 (Figure 6c and d). As expected the efficiencies are lower compared to previous work due to the missing ZnO:Al/Ag back contact [2, 26]. But as mentioned before this study focuses on the influence of the interfaces of the silicon solar cells and the titanium dioxide passivation layer. It can be seen that the integrated devices in the concentrated electrolyte solutions are less stable, which may be related to a faster degradation of the TiO_2 passivation layer. Overall, it can be summarized that the performance of the triple cell is better than that of the tandem cell for all measured pH values. Accordingly, the higher voltage of the a-Si:H/a-Si:H/μc-Si:H triple cell is advantageous to perform the water splitting reaction efficiently compared to an a-Si:H/a-Si:H tandem cell in an integrated device.

4 Conclusions

In summary we studied adapted silicon based multi-junction cells protected by ALD TiO_2 coatings for potential applications in solar-driven water splitting. The interface of the multi-junction cells and the TiO_2 passivation layer was studied with XPS. Based on the XPS measurements the electronic structure of the interface of a tandem- and triple-junction photocathode is presented in the form of energy band diagrams. It is evident from these studies that interface related band bending and band energy arrangements may strongly influence the overall performance of the device. Finally, photoelectrochemical measurements of the prepared buried-junction photocathodes were performed including performance and stability tests using Pt as HER and RuO_2/IrO_2 as OER catalysts. It turned out that a degradation process of the protective coating lowers the efficiency of the integrated devices, which is also confirmed by XPS. XPS data show mainly the appearance of the oxidized silica from below the TiO_2 layer. Recent parallel studies included the investigation of the degradation mechanism with spectroscopic and mircroscopic methods [21]. It has to be clarified if other ALD precursors can be used for the preparation of more stable protective TiO_2 coatings with an appropriate doping and passivating properties. Furthermore, the examination of other oxidic passivation layers for silicon based multi-junction cells would be of great interest.

Acknowledgments: Financial support through the DFG priority program SPP 1613 and by the DFG in the framework of the Darmstadt Graduate School of Excellence for Energy Science and Engineering (GSC 1070) is gratefully acknowledged.

References

1. P. P. Edwards, V. L. Kuznetsov, W. I. David, N. P. Brandonc, Energy Policy **36** (2008) 4356.
2. F. Urbain, V. Smirnov, J.-P. Becker, A. Lambertz, F. Yang, J. Ziegler, B. Kaiser, W. Jaegermann, U. Rau, F. Finger, Energ. Environ. Sci. **9** (2016) 145.
3. R. Liu, Z. Zheng, J. Spurgeon, X. Yang, Energ. Environ. Sci. **7** (2014) 2504.
4. T. Wang, Z. Luo, C. Li, J. Gong, Chem. Soc. Rev. **43** (2014) 7469.
5. D. Bae, B. Seger, P. C. Vesborg, O. Hansenb, I. Chorkendorff, Chem. Soc. Rev. **46** (2017) 1933.
6. Y. Lin, R. Kapadia, J. Yang, M. Zheng, K. Chen, M. Hettick, X. Yin, C. Battaglia, I. D. Sharp, J. W. Ager, A. Javey, J. Phys. Chem. C **119** (2015) 2308.
7. C. Ros, T. Andreu, M. D. Hernández-Alonso, G. Penelas-Pérez, J. Arbiol, O. J. R. Morante, ACS Appl. Mater. Interfaces **9** (2017) 17932.
8. R. L. Puurunen, J. Appl. Phys. **97** (2005) 9.
9. S. M. George, Chem. Rev. **110** (2009) 111.

10. K. Welter, V. Smirnov, J. P. Becker, P. Borowski, S. Hoch, A. Maljusch, W. Jaegermann, F. Finger, ChemElectroChem **4** (2017) 2099.
11. V. Smirnov, A. Lambertz, S. Moll, M. Bär, D. E. Starr, R. G. Wilks, M. Gorgoi, A. Heidt, M. Luysberg, B. Holländer, F. Finger, Phys. Status Solidi (a) **213** (2016) 1814.
12. T. Cottre, M. Fingerle, M. Kranz, T. Mayer, B. Kaiser, W. Jaegermann, (not published yet).
13. D. A. Shirley, Phys. Rev. B **5** (1972) 4709.
14. J. Hill, D. Royce, C. Fadley, L. F. Wagner, F. J. Grunthaner, Chem. Phys. Lett. **44** (1976) 225.
15. J. Ziegler, F. Yang, S. Wagner, B. Kaiser, W. Jaegermann, F. Urbain, J.-P. Becker, V. Smirnov, F. Finger, Appl. Surf. Sci. **389** (2016) 73.
16. J. Aarik, A. Aidla, H. Mändar, T. Uustare, Appl. Surf. Sci. **172** (2001) 148.
17. M. Ritala, M. Leskelä, E. Nykänen, P. Soininen, L. Niinistö, Thin Solid Films **225** (1993) 288.
18. J. Klett, J. Ziegler, A. Radetinac, B. Kaiser, R. Schäfer, W. Jaegermann, F. Urbain, J.-P. Becker, V. Smirnov, F. Fingerd, Phys. Chem. Chem. Phys. **18** (2016) 10751.
19. W. Dahlke, S. Sze, Solid-State Electron. **10** (1967) 865.
20. D. A. Muller, T. Sorsch, S. Moccio, F. H. Baumann, K. Evans-Lutterodt, G. Timp, Nature **399** (1999) 758.
21. E. Ronge, T. Cottre, K. Welter, V. Smirnov, N. J. Ottinger, F. Finger, B. Kaiser, W. Jaegermann, C. Jooss, Z. Phys. Chem. (2019).
22. D. Bae, B. Seger, O. Hansen, P. C. K. Vesborg, I. Chorkendorff, ChemElectroChem **6** (2019) 106.
23. M. Pourbaix, Atlas of Electrochemical Equilibria in Aqueous Solutions, 2nd ed., NACE International, Houston, TX (1974).
24. Z. Chen, T. F. Jaramillo, T. G. Deutsch, A. Kleiman-Shwarsctein, A. J. Forman, N. Gaillard, R. Garland, K. Takanabe, C. Heske, M. Sunkara, E. W. McFarland, K. Domen, E. L. Miller, J. A. Turner, H. N. Dinh, J. Mater. Res. **25** (2010) 3.
25. W. Sheng, H. A. Gasteiger, Y. Shao-Horn, J. Electrochem. Soc. **157** (2010) B1529.
26. F. Urbain, V. Smirnov, J.-P. Becker, U. Rau, J. Ziegler, B. Kaiser, W. Jaegermann, F. Finger, Sol. Energy Mater. Sol. Cells **140** (2015) 275.